IOP Publishing Measurement Science and Technology
Meas. Sci. Technol. **31** (2020) 045016 (17pp) https://doi.org/10.1088/1361-6501/ab5cca

Enhanced feature extraction method for motor fault diagnosis using low-quality vibration data from wireless sensor networks

Qing Shu[1], Siliang Lu[1,2,5], Min Xia[3,5], Jianming Ding[4], Jiahao Niu[1] and Yongbin Liu[1,2]

[1] College of Electrical Engineering and Automation, Anhui University, Hefei, Anhui 230601, People's Republic of China
[2] National Engineering Laboratory of Energy-Saving Motor and Control Technology, Anhui University, Hefei 230601, People's Republic of China
[3] Department of Engineering, Lancaster University, Lancaster, LA1 4YW, United Kingdom
[4] Traction Power State Key Laboratory, Southwest Jiaotong University, Chengdu 610031, People's Republic of China

E-mail: lusliang@mail.ustc.edu.cn or m.xia3@lancaster.ac.uk

Received 14 July 2019, revised 17 November 2019
Accepted for publication 28 November 2019
Published 15 January 2020

Abstract

Wireless sensor networks (WSNs), which are usually powered by batteries, have been extensively used in condition monitoring and fault diagnosis of motors. To extend the battery service life, the length of the acquired and transmitted signal should be short and the sampling resolution should be reduced. In this case, the motor signal quality is low, which affects the fault diagnosis accuracy. To address this issue, this study proposes an enhanced feature extraction method for motor fault diagnosis using low-quality vibration signals acquired from a battery-powered WSN node. First, the vibration signal is converted to an image using a wavelet synchrosqueezed transform technique. Second, the constructed image is enhanced using a histogram equalization. Finally, the enhanced image is inputted into a convolutional neural network (CNN) model, and the motor fault type can be recognized from the CNN output. The effectiveness and efficiency of the proposed method are validated by comparing its performance in the brushless direct motor test rig with the performance of several traditional methods. The relationship between the fault diagnosis accuracy and WSN performances is investigated and discussed. The proposed method shows potential applications for remote motor fault diagnosis using the low-quality vibration signal acquired from a WSN node with limited battery capacity.

Keywords: motor fault diagnosis, histogram equalization, WSST, CNN, low-quality vibration data, WSN

(Some figures may appear in colour only in the online journal)

[5] Author to whom any correspondence should be addressed.

1. Introduction

Motors are used to convert electrical energy to mechanical energy. Moreover, they have been extensively used in household appliances and industrial equipment. A motor consists of mechanical (e.g. bearing, rotor shaft and shell) and electrical components (e.g. rotor and stator winding). After long hours of operation, a motor is prone to various faults due to overload, overheat, intensive vibration and performance degradation. Thus, condition monitoring and fault diagnosis are necessary to guarantee the safe operation of the motor and entire equipment [1–3].

Common motor faults are typically mechanical and electrical in nature. Typical mechanical faults include bearing fault, rotor unbalance and bolt looseness, whereas common electrical faults include interturn fault, interphase fault, high resistance connection and sensor fault [4]. Some faults, such as bearing fault, progress slowly and therefore must be monitored and maintained when necessary [5–9]. Other faults, such as sensor fault, may occur suddenly and must be detected and processed immediately.

To perform effective motor condition monitoring and fault diagnosis, motor signals, including motor current, strain, vibration and acoustic signal, must be acquired, transmitted and processed continuously. These signals are acquired from the distributed sensors and then transmitted to the central data processing. The signal features are extracted and fused to make maintenance decisions.

Recently, deep learning techniques have been developed and extensively applied to fault diagnosis [10–18]. In contrast to the traditional feature extraction and fusion method, deep learning can automatically extract hierarchal features from different layers [19]. This characteristic improves the efficiency of feature extraction and accuracy of pattern recognition. For instance, a novel convolutional neural network (CNN)-based fault recognition method through image fusion of multi-vibration signals was proposed [20], and a deep decoupling CNN was presented for intelligent compound fault diagnosis [21]. A contractive autoencoder was developed to extract discriminative features for machine fault diagnosis [22]. A two-stage method based on unsupervised feature learning was proposed for the intelligent diagnosis of machines [23]. The proposed deep learning methods present superior performance in fault diagnosis.

The performance of the deep learning techniques mainly depends on the model and data [24]. Most studies have focused on optimizing the deep learning models to further improve the accuracy. In addition to the model, data are crucial for deep learning because the accuracy of the model parameters significantly depends on the volume of the training data set. At present, an increasing number of sensors are installed to monitor the motors, and data volume increases rapidly. The massive data benefits the usage of the deep learning techniques and increases the storage space, transmission bandwidth and computation resources.

Another technique called the Internet of Things (IOT) has been rapidly developing in recent years. Through this technique, numerous distributed sensors can be installed on remote areas, and the data can be collected using wireless sensor networks (WSNs) [25]. Figure 1 illustrates an industrial motor and an installed WSN node. Two accelerometers are installed on two ends of the motor to obtain the vibration signals. The signals are transmitted to a remote server through general packet radio service networks. The WSNs are usually powered by batteries. To extend the service life of the battery, signal acquisition and transmission are performed in intermittent mode. For instance, a signal with the duration of 1 s is acquired and transmitted, and then the WSN goes into sleep mode to reduce power dissipation. After a period of time, such as 1 h, the WSN goes into the working mode to acquire and transmit another signal with 1 s length. Such a procedure is shown in figure 2. In this case, a battery may be used for several years, depending on the working conditions. From another aspect, the length of the sample data will affect the service life of the battery. As the power of signal acquisition and transmission is a constant value, reducing the data length can reduce the energy consumption of every working cycle and finally extend the service life of the battery, as illustrated in the top and bottom subfigures in figure 2. Besides, in considering the cost and power consumption, the analog-to-digital converter (ADC) on the WSN usually has low resolution.

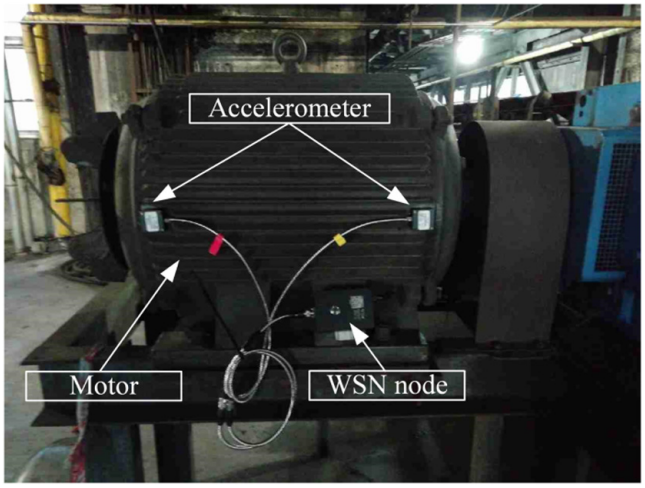

Figure 1. Industrial motor monitored by a WSN node.

Hence, the signal acquired from the WSN is usually of low quality, which will affect the accuracy of motor fault diagnosis. Given this, the application of deep learning techniques to improve the accuracy of motor fault diagnosis when the data quality of the WSN is low is a favorable but challenging topic of interest. This topic has rarely been investigated in the literature. Thus, this study proposes an enhanced feature extraction method for motor fault diagnosis using the vibration data acquired from a WSN node. First, a WSN node is designed, and the vibration signal of the motor is acquired and transmitted to the data processing center. A 1D vibration signal is transferred to a 2D image using the time–frequency analysis (TFA) method. Second, the contrast ratio of the generated image is enhanced through the histogram equalization method. Finally, the enhanced image is inputted into the designed CNN model for motor fault type classification.

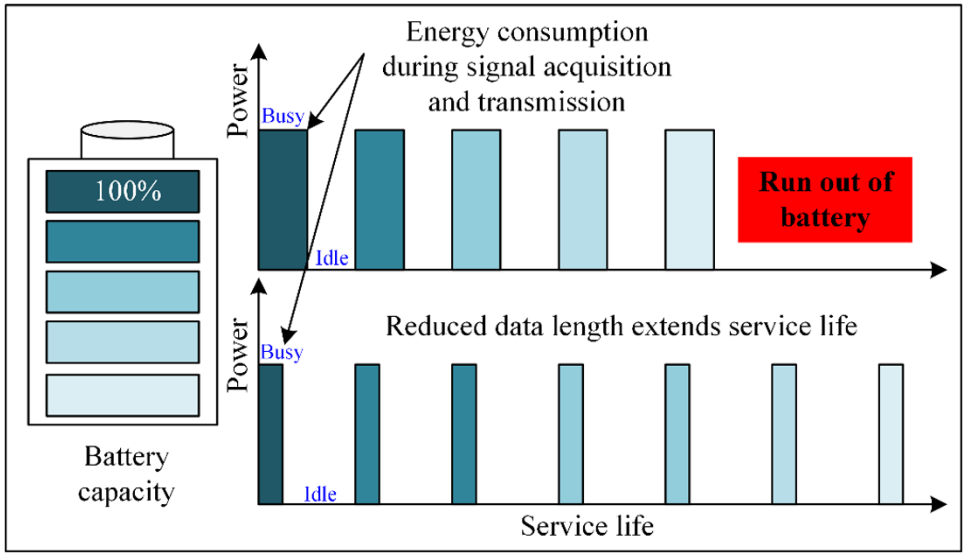

Figure 2. Illustration of the relationship between the signal length and battery service life.

The performance of the proposed method is validated on a brushless direct current motor (BLDCM) platform, which consists of eight motors with different fault conditions. The proposed methods are compared with several traditional methods to illustrate their superiority. The contributions of this study include three aspects: (1) how the signal length and data resolution affect the signal quality and fault diagnosis performance is investigated; (2) focusing on the low-quality vibration signal from a WSN node, an enhanced method is proposed for improving the fault diagnosis accuracy; (3) based on the designed WSN node, the relationship among the signal length, transmission time, consumed power and classification accuracy is evaluated and discussed. By combining deep learning and IOT techniques, the proposed method demonstrates potential applications in fault diagnosis of motors installed in remote areas.

The remainder of this paper is organized as follows. Section 2 introduces the proposed method. Section 3 describes the experimental setup. Section 4 analyzes the features of the motor vibration signals acquired from the WSN node. Sections 5 and 6 validate the effectiveness and efficiency of the proposed method. Section 7 provides the conclusions drawn from this study.

2. Proposed method

In this study, an enhanced feature extraction method is proposed to process the WSN vibration signal from a motor for fault diagnosis. The method consists of three steps as follows: (1) construction of a CNN input image through wavelet synchrosqueezed transform (WSST); (2) image enhancement using histogram equalization; and (3) motor fault type recognition using CNN. The theories related to these procedures are presented subsequently. The implementation and intuitional explanation of these steps are further introduced in the experimental results in sections 5 and 6.

2.1. Image construction through WSST

The CNN model is commonly used in image classification. Considering that the original motor vibration signal is 1D, the vibration signal is transferred to a 2D image to obtain the CNN input signal. In recent decades, many TFA methods, such as short-time Fourier transform (STFT), wavelet transform, Hilbert transform and other variations, have been proposed. In the present study, to construct the image signal, the WSST method is used given its high accuracy and resolution [26, 27]. In what follows, the basis of the WSST theory is briefly introduced.

The motor vibration signal can be considered a continuous signal with multiple components, expressed as

$$S(t) = \sum_{i=1}^{k} A_i(t)\cos\omega_i(t) + e(t), \tag{1}$$

where $A_i(t)$ and $\omega_i(t)$ represent the instantaneous amplitude and frequency of the ith component of the vibration signal, respectively. $e(t)$ denotes the noise or measurement error. The coefficients of the continuous wavelet transform (CWT) of $S(t)$ can be calculated as

$$W_S(a,b) = a^{-1/2}\int S(t)\psi^*\left(\frac{t-b}{a}\right)\mathrm{d}t, \tag{2}$$

where $\psi^*(\cdot)$ is the conjugation function of the mother wavelet $\psi(\cdot)$, and a and b correspond to the wavelet scale and shift factors. For any point combination (a, b), if $W_S(a,b) \neq 0$, then the instantaneous frequency $f_S(a, b)$ can be obtained as

$$f_S(a,b) = -i(W_s(a,b))^{-1}\frac{\partial}{\partial b}W_s(a,b). \tag{3}$$

$f_S(a, b)$ constructs a mapping relationship from (b, a) to $(b, f_S(a, b))$, and the time–frequency representation can be written as [28]

$$T_S(f,b)=\int_{\{a:W_S(a,b)\neq 0\}} W_S(a,b)a^{-3/2}\frac{1}{\delta}h\left(\frac{f-f_S(a,b)}{\delta}\right)\mathrm{d}a, \tag{4}$$

where $h(\cdot)\in C_0^{\infty}$ is a smooth function that satisfies $\|h\|_{L^1}=1$, and δ is the accuracy. If δ is sufficiently small, this operator can be regarded as a partial inversion of the CWT of f over the scale a. In this condition, only the small bands around level curves in the time-scale plane where $f_S(a,b)\approx f$ are taken over and the rest of the plane is ignored. If $\delta\to 0$, the domain of the inversion tends to concentrate on the level curves, i.e. $(a,b):f_S(a,b)=f$. Such a localization process is beneficial to recover the signal component more accurately than inverting the CWT over the entire time-scale plane. Using the WSST, the 1D vibration signal $S(t)$ is transferred to a 2D image $T_S(f,b)$.

However, the energies of the vibration signal are constantly located at a specific bandwidth. From the perspective of an image, bright pixels locate a local area, and other dark pixels locate other areas. In particular, the contrast ratio of the time–frequency image is low, thereby leading to ineffectively distinguishing the images' CNN features and low CNN classification accuracy. Thus, the generated image is further enhanced through the histogram equalization method.

2.2. Image enhancement through histogram equalization

Histogram equalization aims to determine a nonlinear transformation $M(\cdot)$ expressed as [29]

$$g(x,y)=M(c(x,y)), \tag{5}$$

where $g(x,y)$ and $c(x,y)$ are the output and input images, respectively. First, the case of the continuous image is analyzed. Suppose that the values of the normalized images satisfy $0\leqslant g(x,y)\leqslant 1$, and $0\leqslant c(x,y)\leqslant 1$. $M(\cdot)$ is differentiable, increasing and invertible, and the following equation is obtained:

$$c(x,y)=M^{-1}(g(x,y)). \tag{6}$$

The probability density functions (PDFs) of $c(x,y)$ and $g(x,y)$ can be denoted as $p_c(c)$ and $p_g(g)$, respectively. $p_g(g)$ can be obtained using the following equation:

$$p_g(g)=\left[p_c(c)\frac{\mathrm{d}c}{\mathrm{d}g}\right]_{c=M^{-1}(g)}. \tag{7}$$

The transformation function can be defined by rewriting equation (5) as

$$g(x,y)=M(c(x,y))=\int_0^c p_c(\alpha)\mathrm{d}\alpha, \tag{8}$$

in which α is an integration variable, the term $\int_0^c p_c(\alpha)\mathrm{d}\alpha$ is the cumulative distribution function of $c(x,y)$. In addition, a derivation equation can be obtained as

$$\frac{\mathrm{d}g}{\mathrm{d}c}=\frac{\mathrm{d}M(c(x,y))}{\mathrm{d}c}=p_c(c). \tag{9}$$

Substituting equation (9) into (7), the following equation is obtained as

$$\begin{aligned}p_g(g)&=\left[p_c(c)\frac{\mathrm{d}c}{\mathrm{d}g}\right]_{c=M^{-1}(g)}=\left[p_c(c)\frac{1}{\mathrm{d}g/\mathrm{d}c}\right]_{c=M^{-1}(g)}\\&=\left[p_c(c)\frac{1}{p_c(c)}\right]=1.\end{aligned} \tag{10}$$

It can be noticed that the PDF of the variable $g(x,y)$ is uniformly distributed. Hence, by using the cumulative distribution function as the transformation function, a grayscale image with uniformly distributed levels can be obtained. In other words, the dynamic range of the image is improved by histogram equalization.

In accordance with the abovementioned derivations, the discrete form of histogram equalization can be obtained. Assume that the discrete grayscale image $c[x,y]$ has L gray levels, and the discrete amplitude values of $c[x,y]$ are c_0, c_1,…, c_{L-1}. The discrete statistical probabilities for different gray levels are expressed as

$$P_i=\frac{n_i}{N}, i=0,1,...,L-1, \tag{11}$$

where n_i is the pixel count for gray level i, and N is the total number of pixels. Finally, the discrete approximation of equation (8) can be written as

$$g_k=M[c_k]=\sum_{i=0}^{k}P_i, k=0,1,...,L-1. \tag{12}$$

The values of g_k fall in the range of [0, 1] and may have to be rounded and scaled appropriately. Through histogram equalization, the histogram of the original time–frequency image is re-distributed, and thus the contrast ratio along with the CNN classification accuracy will be improved.

2.3. CNN for motor fault type recognition

CNN models have been confirmed effective in image recognition and classification [30, 31]. In the present study, 1D vibration signals are converted to 2D images. Then, these 2D images are enhanced to increase the contrast rates. The enhanced images are then processed using the CNN model. Finally, the motor signals with different fault types can be recognized [32]. A CNN model constantly consists of multiple layers, namely, input, convolutional, batch normalization, rectified linear unit (ReLU), pooling, fully connected, and output layers (figure 3). The detailed functions and parameters of the layers are presented below.

The convolutional layer in a CNN model can be expressed as

$$X_j^l=f\left(\sum_{i\in M_j}X_i^{l-1}*k_{ij}^l+b_j^l\right), \tag{13}$$

where l represents the current layer number, M_j is a collection of input features from the previous layer, X_j^l represents the jth feature map generated from the lth layer and k_{ij}^l represents the jth kernel, which connects with the ith input feature map. Moreover, $f(\cdot)$ denotes an activation function, b_j^l represents the bias that corresponds to the jth kernel and $*$ represents the 2D convolution operation.

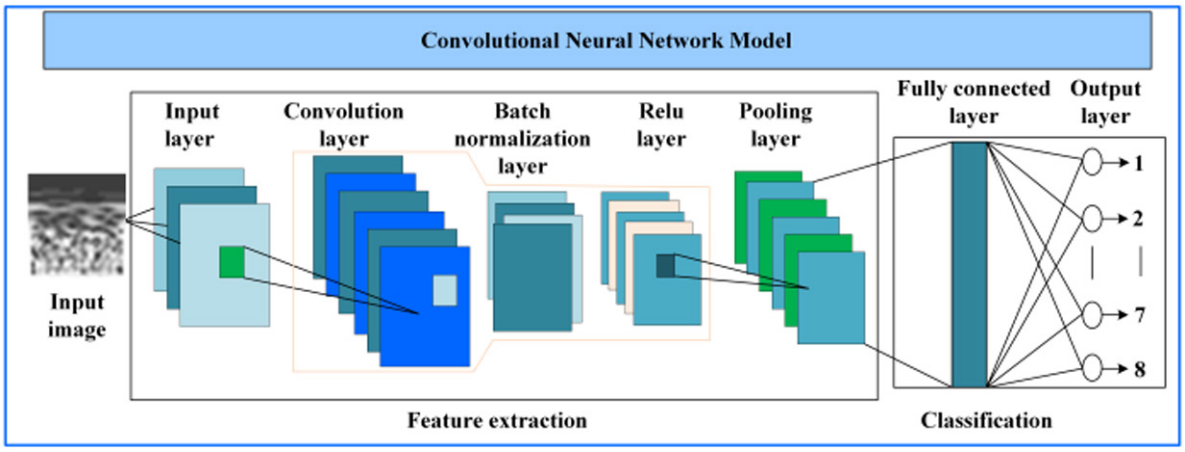

Figure 3. Illustration of the CNN model.

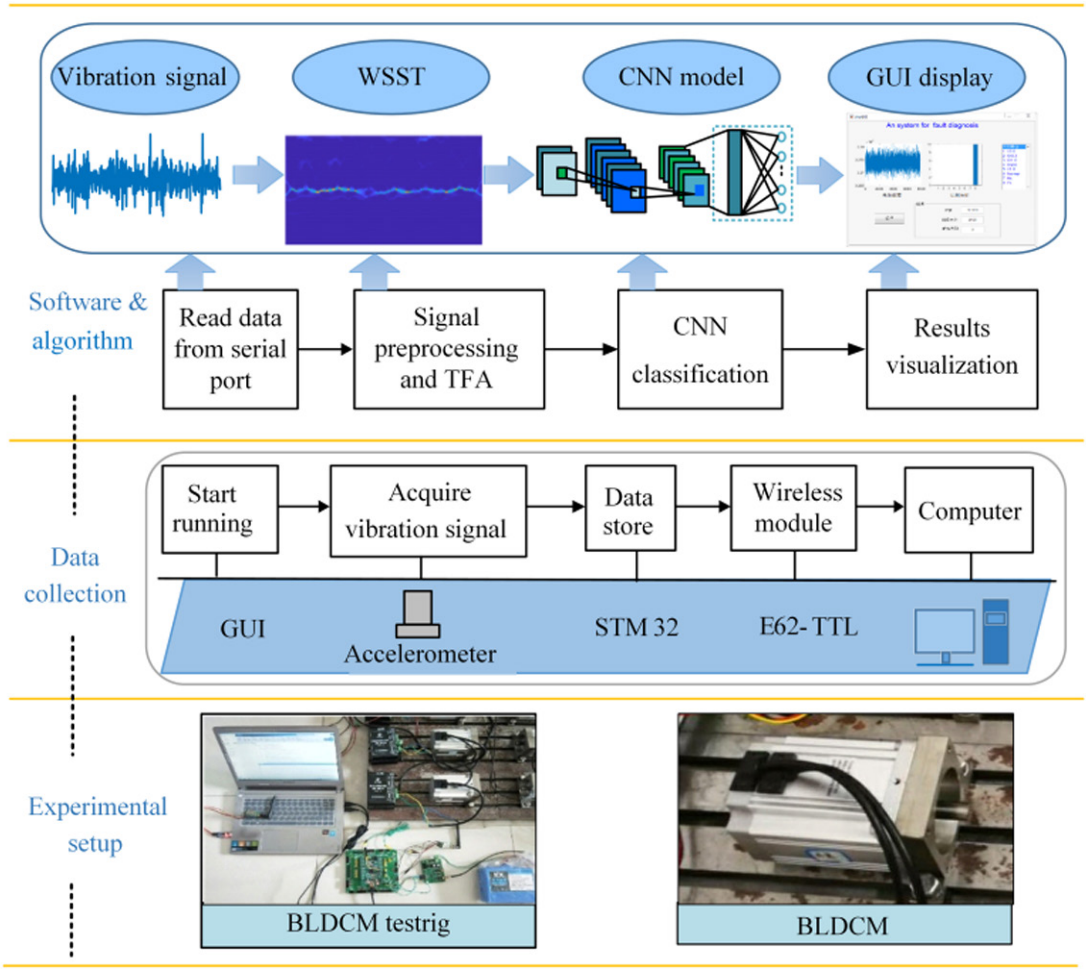

Figure 4. Experimental setup and WSN system.

The batch normalization layer is used to decrease the internal covariance shift and accelerate the training process of the CNN. This layer is typically added after the convolution layer or the fully connected layer expressed as

$$\hat{x}^{(i)} = \frac{x^{(i)} - E\left[x^{(i)}\right]}{\sqrt{\mathrm{Var}\left[x^{(i)}\right]}}, \tag{14}$$

$$y^{(i)} = \gamma^{(i)}\hat{x}^{(i)} + \beta^{(i)}, \tag{15}$$

where $\hat{x}^{(i)}$ is the normalized form of $x^{(i)}$, $y^{(i)}$ is the output of one neuron response, and $\gamma^{(i)}$ and $\beta^{(i)}$ represent the scale and shift parameters to be learned, respectively.

The activation function aims to construct a mapping from the original linear indivisible multi-dimensional features to another space where the linearity of the features can be enhanced. In the present study, the commonly used ReLU activation function is adopted. The formula of ReLU is

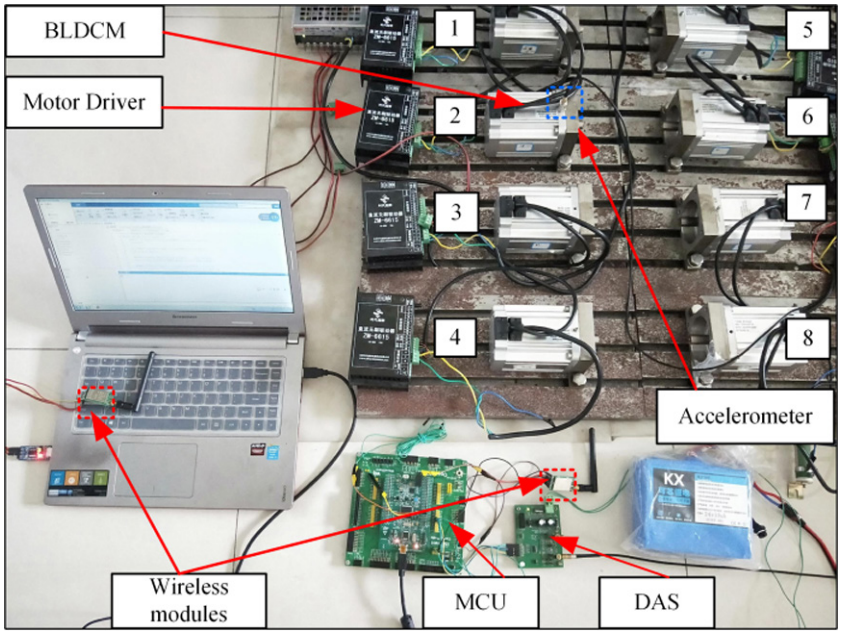

Figure 5. Experimental setup.

Table 1. Parameters of the BLDCM.

Motor type	Rated voltage	Rated power	No. of pole pairs	No. of phases
80BL110S50	48 VDC	500 W	2	3

Table 2. Description of the motor fault types.

Motor condition	No. of training/ testing samples	Label
Inner raceway fault/2.0 mm	1000/100	1
Outer raceway fault/0.3 mm	1000/100	2
Outer raceway fault/1.0 mm	1000/100	3
Outer raceway fault/2.0 mm	1000/100	4
Inner raceway fault/1.0 mm	1000/100	5
Normal condition	1000/100	6
Hall sensor fault	1000/100	7
Rotor eccentricity	1000/100	8

$$a_i^{l+1}(j) = f\left(y_i^{l+1}(j)\right) = \max\left\{0, y_i^{l+1}(j)\right\}, \quad (16)$$

where $y_i^{l+1}(j)$ represents the output of the 2D convolution operation and $a_i^{l+1}(j)$ represents the activation of $y_i^{l+1}(j)$.

The pooling layer is mainly used to reduce the parameters of the CNN. The maximum pooling method is adopted in this study. This method takes the maximum value in the sensing domain as the output, and the obtained features are independent of the positions. The maximum pooling can be expressed as

$$p_i^{l+1}(j) = \max_{(j-1)W+1 \leqslant t \leqslant jW} \left\{q_i^l(t)\right\}, \quad (17)$$

where $q_i^l(t)$ represents the value of the ith neuron in the frame of the lth layer, $t \in [(j-1)W+1, jW]$, W represents the width of the pooling window and $p_i^{l+1}(j)$ represents the corresponding value of the neuron in the $(l+1)$th layer of the pooling operation. By using the CNN, the time–frequency features involved in the enhanced images are extracted, and hence motor fault types can be distinguished.

3. Experimental setup and WSN system design

To verify the performance of the proposed method, an experimental setup and a WSN system are designed, as depicted in figure 4.

3.1. Experimental setup

The experimental setup is demonstrated in figure 5. In this figure, eight BLDCMs with different fault types are tested. The detailed parameters of the BLDCM and the fault types are listed in tables 1 and 2, correspondingly.

3.2. WSN system: hardware design

A WSN system is designed to acquire the motor vibration signal and transmit the signal to a computer for motor fault recognition and result statistics. The hardware circuit of the WSN is exhibited in figure 6. An accelerometer (CA-YD-1182, SINOCERA, Inc.) is installed on the driving end of the motor to acquire the vibration signal. The signal is sampled and quantized using a 16-bit ADC (Max1300, MAXIM, Inc.). The ADC is controlled by a microcontroller unit (MCU, STM32F407, STMicroelectronics, Inc.) through a serial peripheral interface. Two wireless modules (E62-TTL-100), that is, one receiver and one transmitter, are used to transmit the data from the WSN to a computer. The wireless modules communicate with the MCU and an adapter through a universal

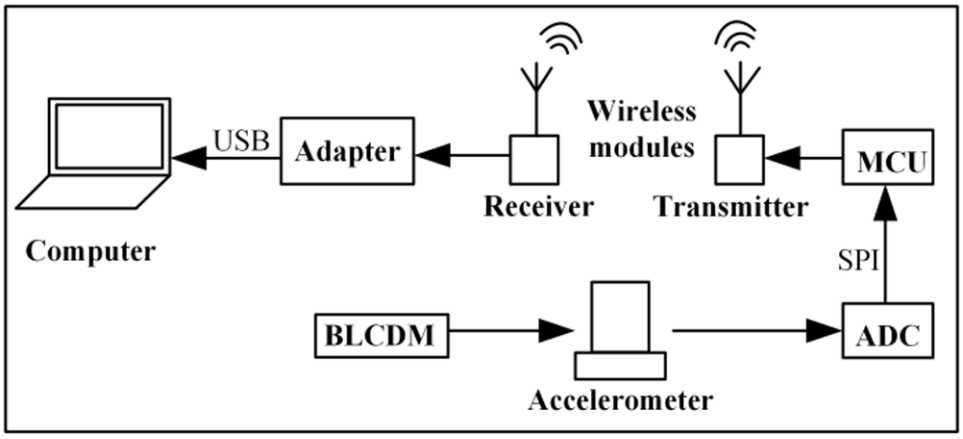

Figure 6. Hardware circuit of the WSN system.

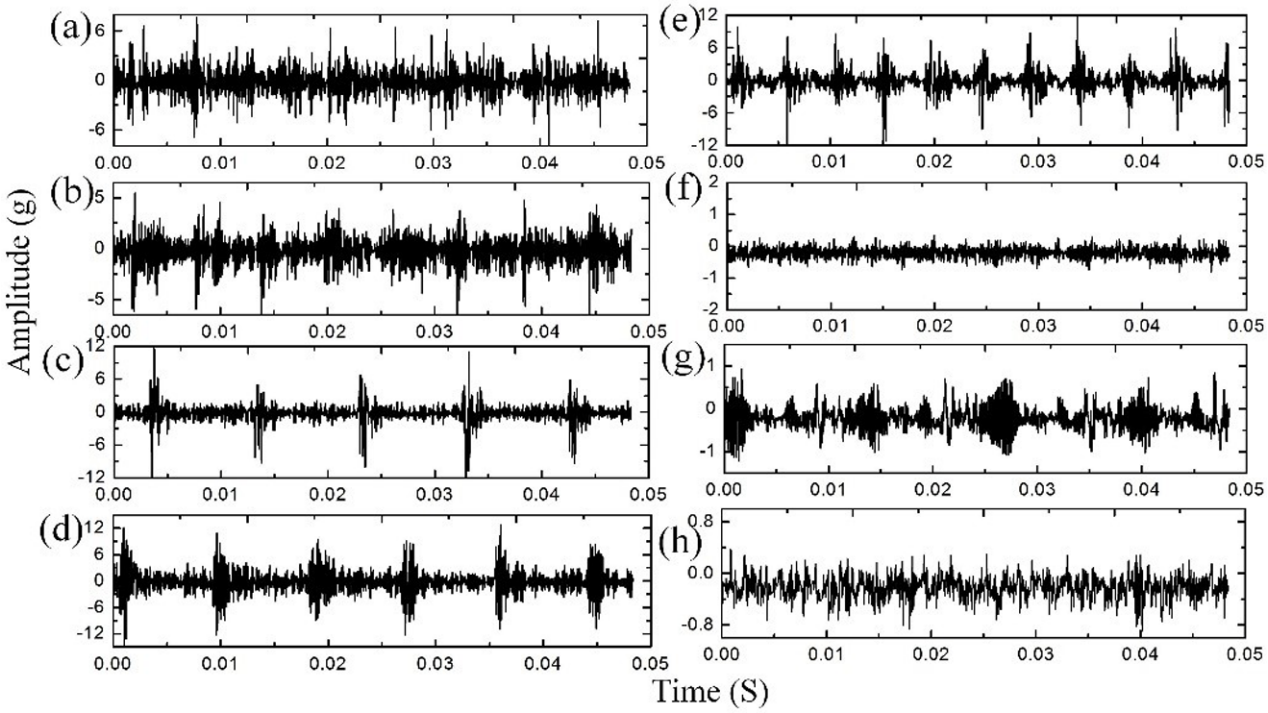

Figure 7. Time-domain waveforms of the motor vibration signals: (a) inner raceway fault/2.0 mm, (b) outer raceway fault/0.3 mm, (c) outer raceway fault/1.0 mm, (d) outer raceway fault/2.0 mm, (e) inner raceway fault/1.0 mm, (f) normal condition, (g) Hall sensor fault, and (h) rotor eccentricity.

synchronous asynchronous receiver transmitter (USART) interface. The adapter transfers the USART interface to a universal serial bus interface to connect with the computer. First, the data with eight types of motor conditions are acquired by the WSN and transmitted to the computer. These storage data form an offline database on the computer. The database is used to illustrate the method procedure and performance in section 4 and also used for training the CNN model. After training, the new data are acquired and transmitted frame by frame to the computer for online fault recognition.

3.3. WSN system: algorithm flowchart

The algorithm flowchart for motor fault diagnosis through the proposed CNN method and the designed WSN is displayed in figure 4.

Step 1: The motor vibration signal is acquired using the designed WSN node, and the sampling frequency is set to 20 kHz. The signal is transmitted to the computer.
Step 2: The 1D vibration signal is converted to a 2D image through the WSST technique.
Step 3: The generated 2D image is enhanced through the histogram equalization method, and the contrast ratio of the image is improved.
Step 4: The enhanced 2D image is sent to the well-trained CNN model, and then the bearing fault can be recognized from the CNN output.

Considering that this study focuses on the WSN-based motor fault diagnosis, the relationship between the fault diagnosis accuracy and WSN performance is evaluated. Thus, the signal transmission time and consumed energy are measured

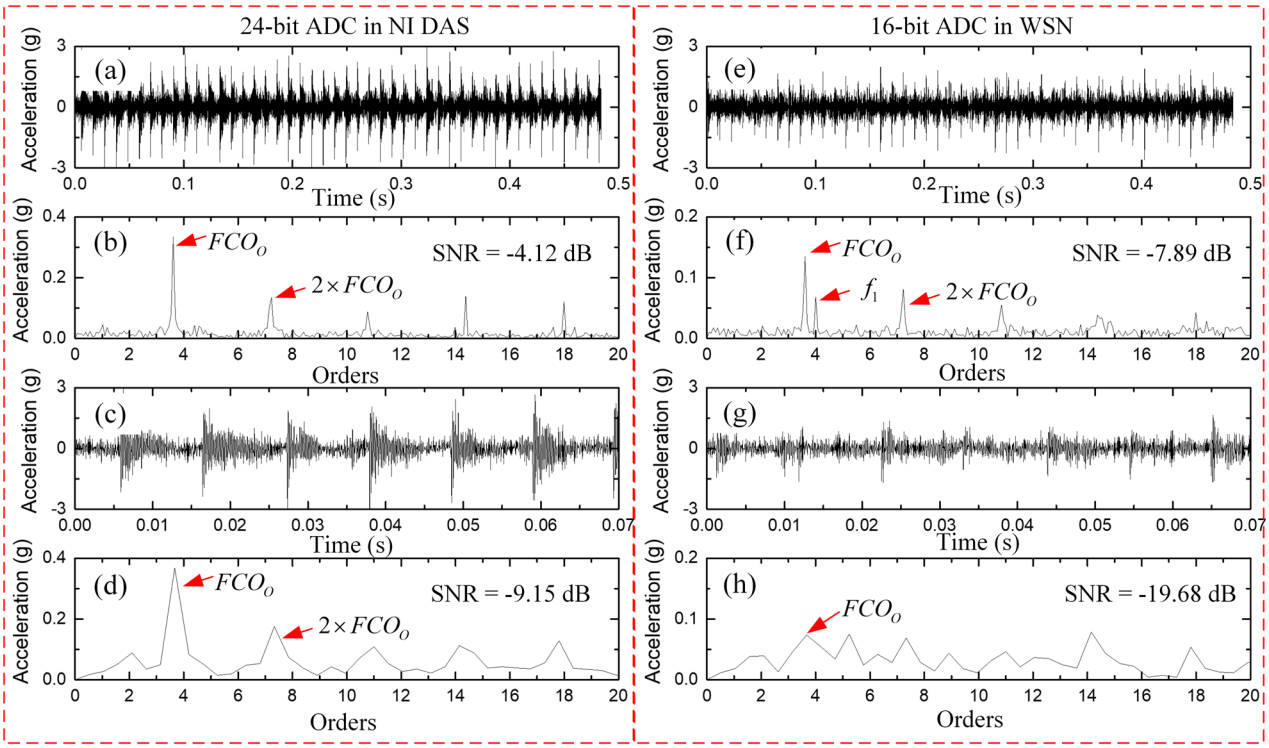

Figure 8. Effects of signal length and data resolution for motor bearing fault diagnosis with a sampling frequency of 20 kHz: (a) 9680 sampling points in 24-bit and (b) its envelope order spectrum; (c) 1452 sampling points in 24-bit and (d) its envelope order spectrum; (e) 9680 sampling points in 16-bit and (f) its envelope order spectrum; (g) 1452 sampling points in 16-bit and (h) its envelope order spectrum.

and displayed using the graphical user interface on the computer screen (figure 4).

4. Features of the motor vibration signals acquired from WSN node

4.1. Motor vibration signal waveforms

The motor vibration signals with a length of 968 sampling points acquired from the test rig are illustrated in figure 7. Figures 7(a)–(h) correspond to fault types 1–8 listed in table 2. When an outer raceway fault appears in the motor bearing, the fault-induced impulses can be observed in the waveforms, as depicted in figures 7(b)–(d). When an inner raceway fault occurs, the impulses and waveform fluctuations are observed in the signals, as demonstrated in figures 7(a) and (e). For the normal motor without fault, the signal amplitude is lower than that of the fault signals, as exhibited in figure 7(f). A Hall sensor fault that occurs in the motor will result in a commutation delay in the motor driver and further lead to unstable rotation. Thus, a periodic fluctuation will occur, as presented in figure 7(g). The rotor eccentricity signal is displayed in figure 7(h). The signal amplitude is higher than that of the normal signal because eccentricity induces intensive vibration.

4.2. Signal features analysis

In this subsection, the features of the vibration signals acquired from the WSN node are further analyzed, and the relationship among the signal length, data resolution and fault diagnosis effect is investigated. Envelope spectral analysis is a commonly used technique to analyze the vibration signal features. For instance, when a localized fault occurs in a motor bearing, the fault characteristic order (FCO), which is the ratio of the fault characteristic frequency and rotation frequency, will appear in the envelope order spectrum. The motor bearing signal with the outer raceway fault is used as an example. According to the bearing type (6002Z) and bearing parameters (outside diameter: 32 mm, inside diameter: 15 mm, number of rollers: 9), the FCO at the outer raceway fault (denoted as FCO_O) is calculated as 3.59 [33]. Besides, the data resolution of the ADC in the WSN node is 16-bit, as introduced in section 3.2. To evaluate how the data resolution affects the motor fault diagnosis, the vibration signal with the bearing outer raceway fault is sampled by another commercial data acquisition system (DAS, USB4432, NI, Inc.) with 24-bit ADC resolution for comparison.

The results for different signal length and data resolution are shown in figure 8. The subfigures in the left column show the signals acquired from the NI DAS with 24-bit ADC resolution and their corresponding envelope order spectra. In figure 8(b), the spectrum is calculated from the signal with a length of 9680 sampling points, and the fault indicator FCO_O and its harmonics such as $2 \times FCO_O$ can be clearly seen in the spectra. Such a result confirms that an outer raceway fault occurs in the motor bearing. When the signal length decreases from 9680 points to 1452 points, the envelope order spectrum is shown in figure 8(d). The FCO_O and $2 \times FCO_O$ components can still be found, but the frequency resolution which equals to the sampling frequency divided by the number of sampling

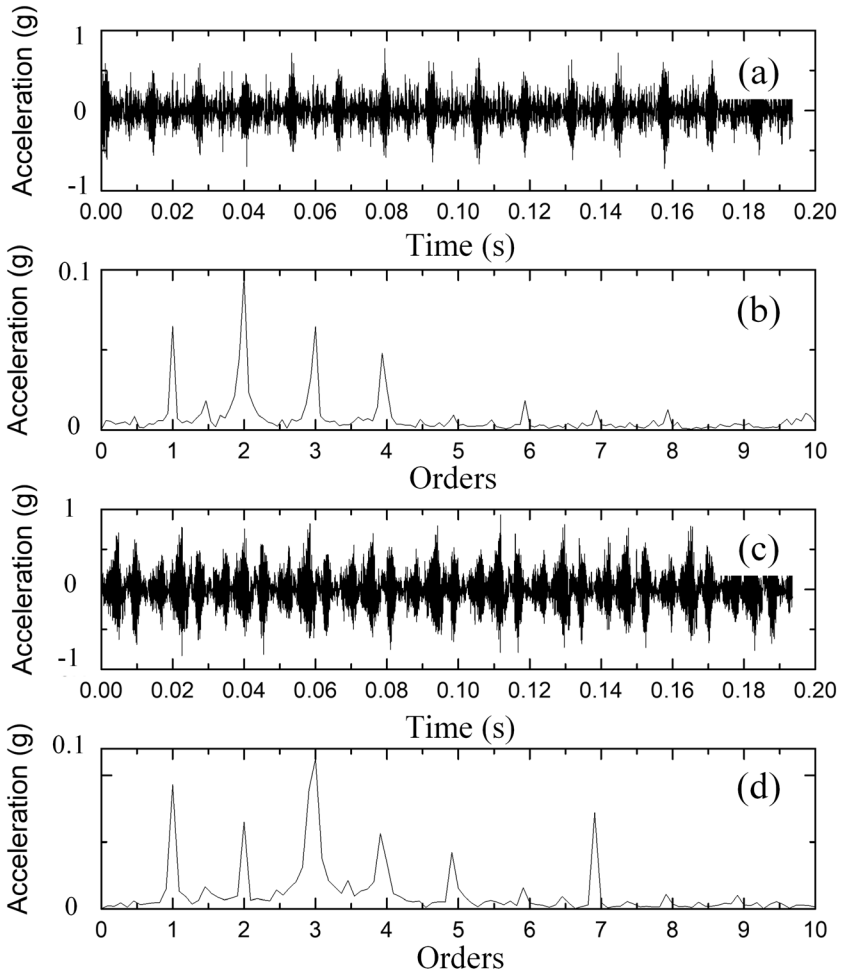

Figure 9. (a) Hall sensor fault signal waveform and (b) its envelope order spectrum; (c) rotor eccentricity signal waveform and (d) its envelope order spectrum.

points, decreases obviously. To quantitatively evaluate the effect of motor bearing fault diagnosis, the signal-to-noise ratio (SNR) is introduced as expressed below:

$$\mathrm{SNR} = 10\log_{10}\frac{\sum_{i=1}^{5} P\left[i \times \mathrm{round}\left(\frac{\mathrm{FCO_O}\times \mathrm{NFFT}}{f_s}\right)+1\right]}{\sum_{i=1}^{\mathrm{NFFT}/2} P[i] - \sum_{i=1}^{5} P\left[i \times \mathrm{round}\left(\frac{\mathrm{FCO_O}\times \mathrm{NFFT}}{f_s}\right)+1\right]}, \tag{18}$$

in which $P[i]$, $i = 1, 2, \ldots,$ NFFT is the discrete spectrum, NFFT is the number of points of fast Fourier transform and f_s is the sampling frequency. The SNR in equation (18) regards $\mathrm{FCO_O}$ and its second to fifth harmonics as useful signals and the other components as noises. The SNR in figures 8(b) and (d) are calculated as −4.12 and −9.15 dB, respectively. In other words, the SNR decreases with the decrease of signal length, and further affects the diagnosis performance.

The waveforms and spectra of the WSN signals from the offline database are shown in the subfigures in the right column of figure 8. The signal length in figure 8(e) is the same as that in figure 8(a). However, the spectrum in figure 8(f) demonstrates that the noise interference is more obvious than that in figure 8(b). For instance, a noise component f_1 with no explicit meaning is close to the $\mathrm{FCO_O}$. The corresponding SNR is calculated as −7.89 dB, which is lower than that from the 24-bit ADC in figure 8(b). Such a result indicates that the ADC resolution affects the accuracy of the extracted features of the vibration signals. Moreover, when the signal has a short length (1452 sampling points) and low data resolution (16-bit), the results are shown in figures 8(g) and (h). The $\mathrm{FCO_O}$ and its harmonics are hardly identified in the spectrum, and the SNR decreases to −19.68 dB. According to the above analyses, it can be found that the WSN signal is usually of low quality due to the limitations of the hardware including limited battery capacity and limited ADC resolution.

As indicated in table 2, the motor fault types include the bearing fault, Hall sensor fault and rotor eccentricity. Different bearing fault types can be distinguished by the FCO indicators [33]. Except for the bearing fault, the waveforms and envelope order spectra of the Hall sensor fault and rotor eccentricity vibration signals are shown in figure 9. The signal length is 3872 sampling points in figures 9(a) and (c). It can be seen in the envelope order spectra that both the Hall sensor fault and rotor eccentricity contain the 1×, 2× and multiple integer harmonics. Indeed, the Hall sensor fault can be regarded as one kind of electrical asymmetry fault, and hence its fault features are similar to those of the mechanical rotor eccentricity. As the magnitudes of these harmonics will vary in different tests, the Hall sensor fault and rotor eccentricity are not easily and

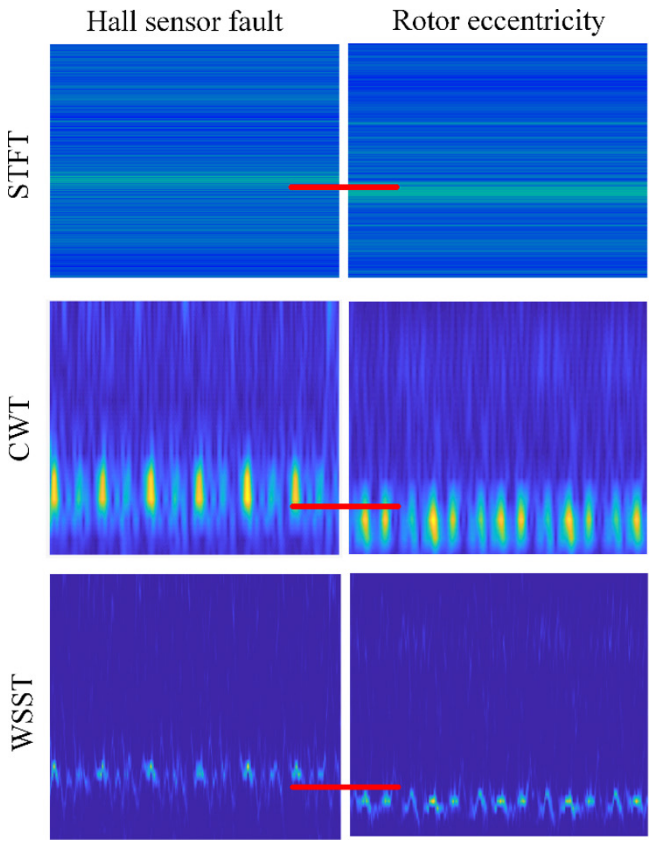

Figure 10. Comparison of the TFA methods in processing the Hall sensor fault and rotor eccentricity signals. Top: STFT; middle: CWT; bottom: WSST.

directly distinguished in the envelope order spectra. In addition, when the signal length decreases further, these two kinds of faults will become more difficult to recognize from the spectrum. Hence, a more effective method should be investigated to distinguish different motor fault types from the WSN signals.

5. Effectiveness evaluation of the proposed method

As indicated in section 4, the quality of the signals from the WSN node is low and hence it is difficult to diagnose the motor fault by using the traditional envelope spectral analysis method. Hence, an improved CNN-based feature extraction and pattern recognition method is investigated in this study. The vibration signals in figure 7 are analyzed to validate the effectiveness of the proposed method for motor fault diagnosis.

5.1. WSST images generated from the vibration signals

In section 2.1, 1D vibration signals are converted to 2D images as the CNN inputs. WSST is an advanced TFA method and it has better performance in characterizing the signal features in the time–frequency plane compared with the traditional methods such as STFT and CWT. A comparison of the TFA methods for analyzing the Hall sensor fault and rotor eccentricity signals is performed and the results are shown in figure 10. The signal length is 1568 sampling points for both signals. The parameters of the STFT are configured as window length 256 points, overlap 250 points and NFFT 256 points. For the CWT and WSST, the bump wavelet is selected and other parameters are defaults in the built-in MATLAB functions. In each subfigure, the x- and y-axes represent the time- and frequency-axis, respectively. The STFT results are shown in the top subfigures, where it can be seen that these two subfigures are similar. The dominant frequency bandwidth locates at the low-frequency region (close to the bottom of the subfigure). However, as the frequency resolution of the STFT method is limited, the dominant bandwidths of two signals are partly overlapped as indicated by a horizontal red line. Such a result decreases the discrimination of the two signals and further affects the diagnosis accuracy of the motor faults. The results from the CWT methods are shown in the middle subfigures in figure 10. The periodic impulses can be seen in the time–frequency plane as indicated by the highlight spots, and the resolution of the time–frequency figure has been improved compared with that of the STFT. However, the overlapping of the dominant bandwidths at the frequency-axis can still be noticed as indicated by a red line. The results from the WSST method are shown in the bottom subfigures in figure 10. It can be found that the energy smearing phenomenon is reduced by introducing the synchrosqueezed transform and hence the features on the time–frequency plane can be better identified. The horizontal red line also indicates that there are no overlapping bandwidths in the two subfigures. In view of pattern recognition, the more different features that exist in the two figures, the better the discrimination. Hence, it is expected that the WSST-based feature extraction method will produce a high accuracy of motor fault diagnosis.

Then, the grayscale WSST images corresponding to the signals in figure 7 are illustrated in figure 11. A dark pixel and a bright pixel represent the low and high energies on the time–frequency plane of the vibration signal, correspondingly. In the generated images, the majority of the energies distribute at the low-frequency region (i.e. the bottom of the image). At the high-frequency region, the time–frequency energies are low, as indicated in the concentrated dark regions at the top of the image. Given the image quality, the image contrast rate is low, thereby decreasing the accuracy of CNN feature extraction and fault recognition.

5.2. Image enhancement using histogram equalization

Histogram equalization is applied to the original image to improve the contrast rate. Figure 12(a) depicts the original image and its gray-level distributions. Based on the image, most of the pixels distribute at low gray levels (i.e. below 50). This image is then enhanced using histogram equalization, and the result is displayed in figure 12(b). The distribution of dark and bright pixels is more homogeneous in the enhanced image than in the original image. Figure 13 demonstrates the respective enhanced versions of the images presented in figure 11. The details and textures of the enhanced images can be identified well. In particular, the image contrast rate has been improved, thus benefiting CNN feature extraction and image classification.

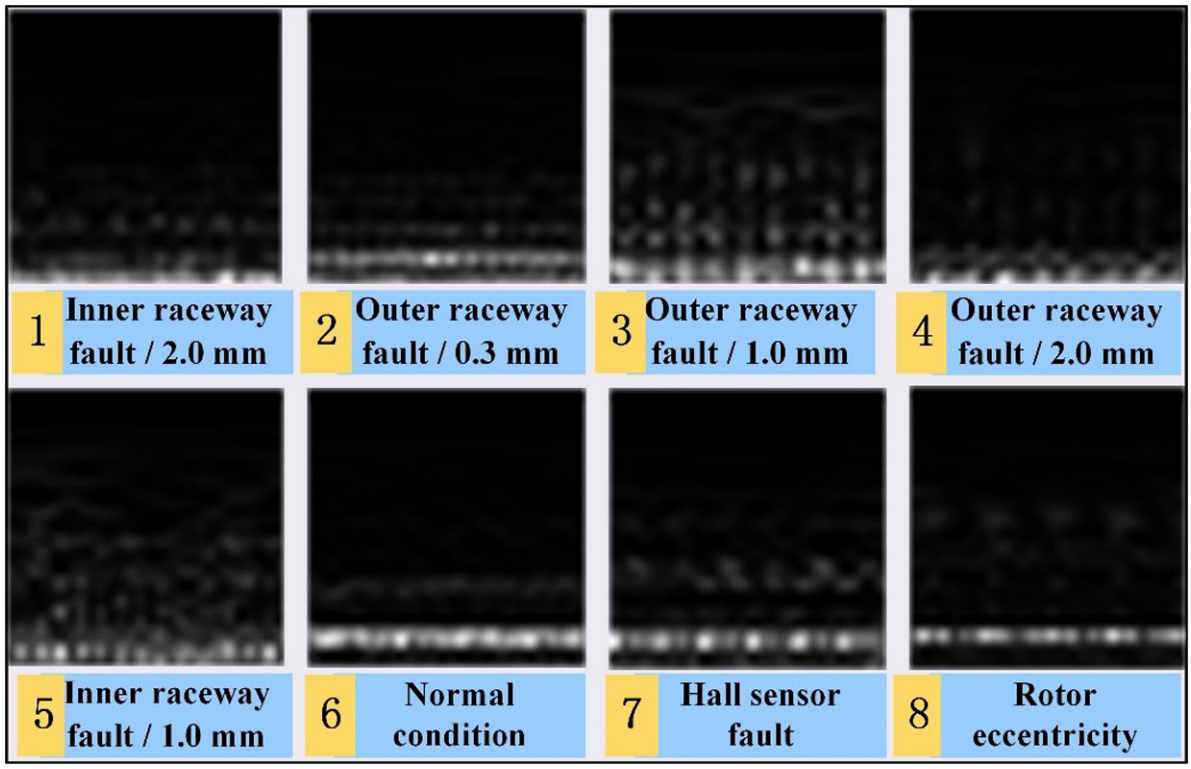

Figure 11. Time–frequency images generated using the WSST.

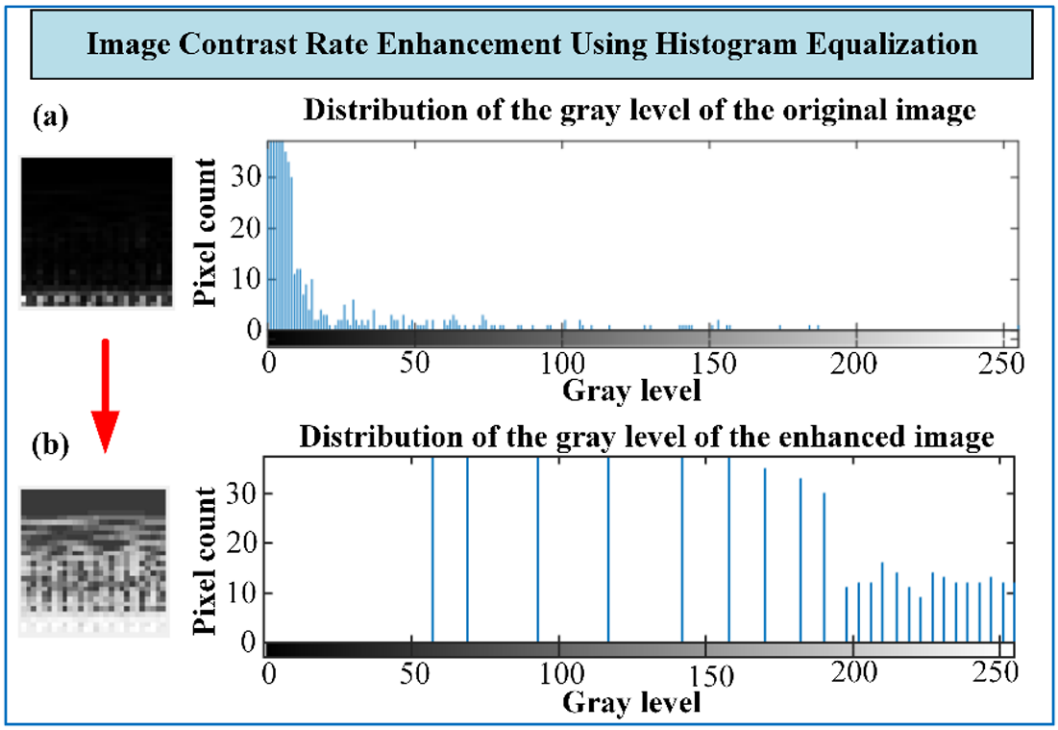

Figure 12. Illustration of image histogram equalization: (a) before and (b) after enhancement.

5.3. Motor fault recognition using CNN

In this study, the CNN model is used to extract the hierarchal features from the enhanced images exhibited in figure 13. Then, the motor fault type can be recognized from the CNN output. The parameters of the CNN model are listed in table 3. Eight kinds of enhanced images that correspond to different motor fault types are used to train the CNN model. Each data set from the offline database comprises a total of 1100 samples for every motor condition. Of these samples, 1000 are used for training, while 100 are utilized for validation (8000 samples are trained and 800 samples are validated). The CNN is trained

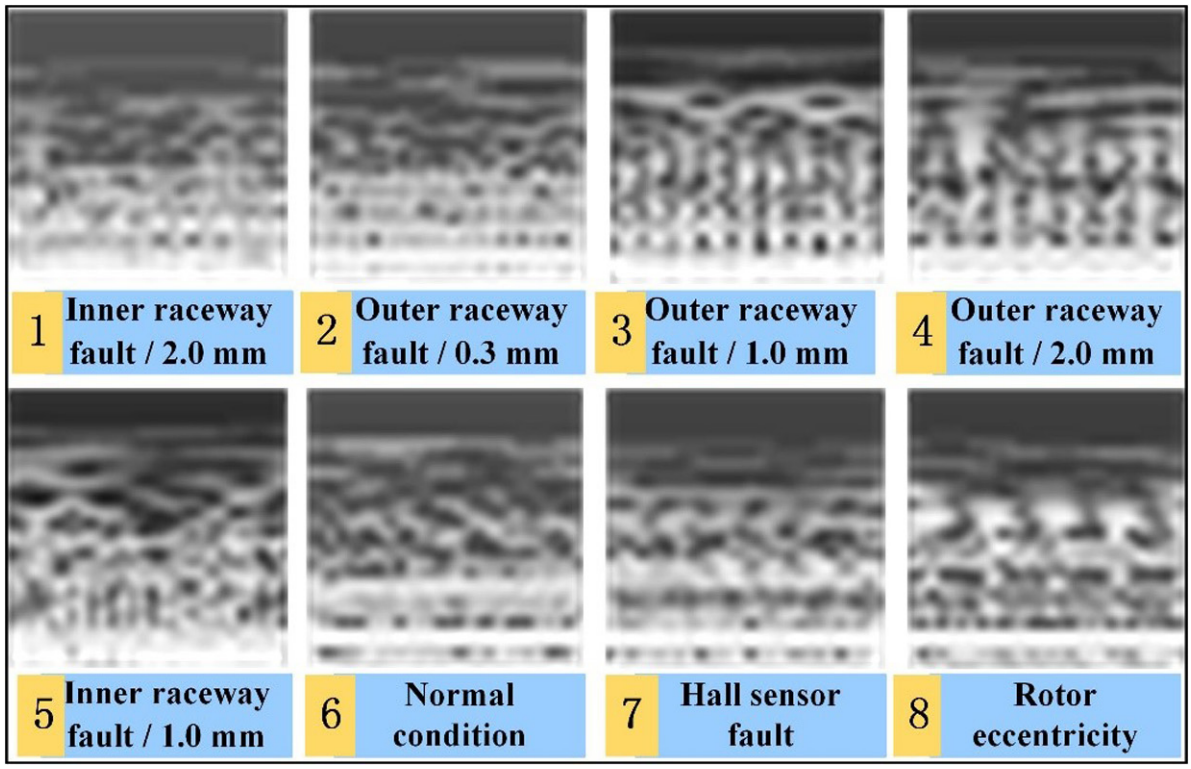

Figure 13. Enhanced images using histogram equalization.

Table 3. Details of the designed CNN Model.

Layer	Layer type	Parameters
1	Input layer	28s × 28 pixels
2	Convolutional layer	Filter size = 3 × 3 pixels, no. of filters = 16
3	Batch normalization layer	—
4	ReLU layer	—
5	Max-pooling layer	Pool size = [2 2], stride = [3 3]
6	Fully connected layer	No. of channels = 8
7	Softmax layer	—
8	Classification layer	No. of channels = 8

using the stochastic gradient descent with momentum with an initial learning rate of 0.01, and the maximum number of epochs is set to three. The other parameters are defaults in the built-in MATLAB functions. In the CNN training and validation (figure 14), the training accuracy is approximately 100%, and the training loss converges to nearly 0 after 40 epochs.

A well-trained CNN model is obtained after 40 epochs of training. To validate the effectiveness of the proposed method, eight kinds of images are selected randomly from the validation data set and inputted into the well-trained CNN model. The results of the predictive and actual fault modes are illustrated in figure 15. The highlighted values are the maximum of each row. In this figure, the maximum probability of the predictive fault modes matches the actual fault modes in each test. The maximum probability ranges from 98.33%–100%, which is significantly larger than other probabilities. The results indicate that the motor fault type is successfully recognized through the proposed method.

6. Efficiency evaluation and discussions

First, the vibration signal acquired from the designed WSN node is converted to an image. Second, the motor fault type can be recognized through the proposed CNN method. The WSN node is constantly powered by a battery with limited capacity, and each signal acquisition and transmission will consume energy. Therefore, decreasing the data length of the acquired signal will reduce the consumed energy and extend the service life of the node. On the other hand, the signal length affects the accuracy of feature extraction and fault recognition because a long signal contains sufficient information relative to the motor condition, and vice versa. Thus, the relationship

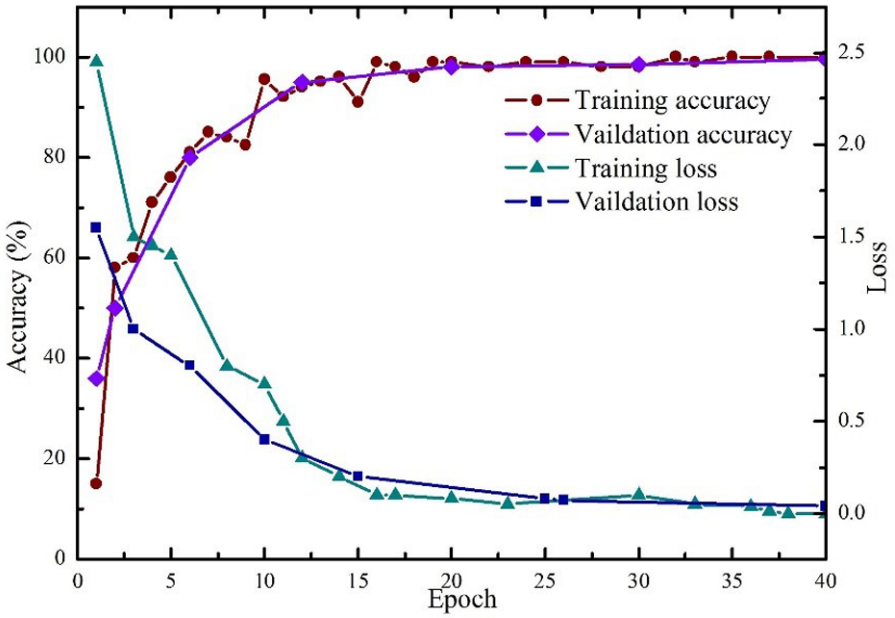

Figure 14. Procedures of the CNN training and validation.

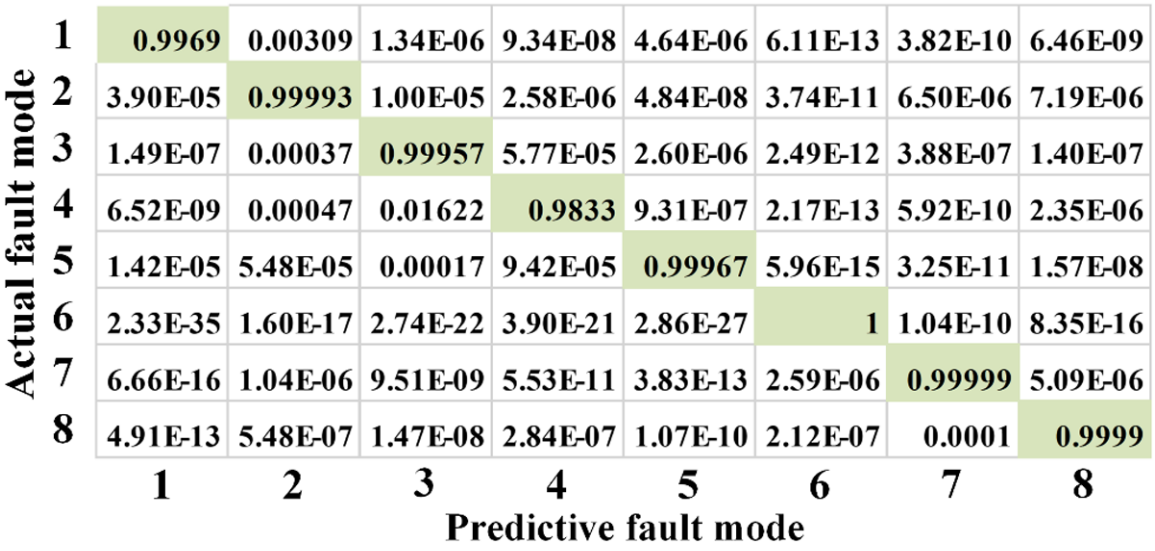

Figure 15. Confusion matrix of the actual and predictive fault modes.

Table 4. Detailed descriptions of the different methods.

Method	Key technique	Detailed description
M1	WSST, histogram equalization	Vibration signal is converted to an image through WSST, image is enhanced through histogram equalization
M2	WSST	Vibration signal is converted to an image through WSST
M3	CWT	Vibration signal is converted to an image through CWT
M4	STFT	Vibration signal is converted to an image through STFT
M5	Signal realignment	1D Vibration signal is realigned to construct a 2D image

between the data length and motor fault recognition rate must be evaluated through the CNN method.

6.1. Method comparison

The proposed method is compared with four other methods in terms of different signal length and image resolution. The details of the different methods are summarized in table 4. M1 represents the proposed method, which is introduced in section 2. M2 is a simplified method of M1 without the histogram equalization procedure. M3 is similar to M2, except that the CWT, rather than the WSST, is used to obtain the 2D image. M4 is also a CNN-based method and the input image is constructed using STFT. Image $I[i, j]$ in method M5 (referred

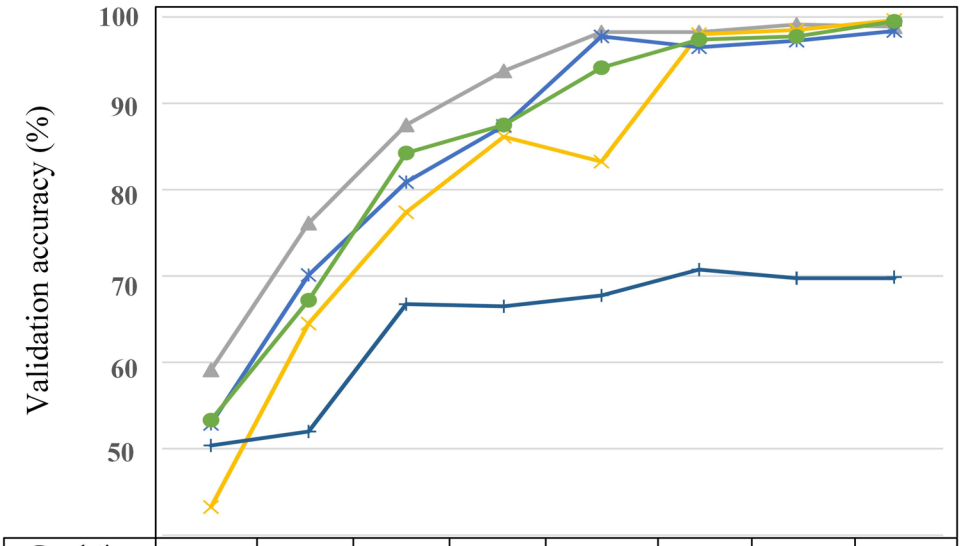

Resolution	7×7	10×10	12×12	14×14	18×18	22×22	26×26	28×28
Signal length	98	200	288	392	648	968	1452	1568
M1	59. 13	76. 13	87. 5	93. 75	98. 25	98. 25	99. 13	98. 88
M2	43. 25	64. 5	77. 38	86. 13	83. 25	98	98. 5	99. 63
M3	52. 88	70. 12	80. 88	87. 38	97. 75	96. 5	97. 25	98. 38
M4	53. 38	67. 25	84. 25	87. 5	94. 13	97. 38	97. 75	99. 5
M5	50. 38	52	66. 75	66. 5	67. 75	70. 75	69. 75	69. 88

Figure 16. Comparison between the proposed method M1 and other methods.

from [34]) is constructed directly from the original vibration signal $S[n]$ and is expressed as

$$I[i,j] = S[(i-1) \times K_1 + j], i = 1, 2, ..., K_2, j = 1, 2, ..., K_1, \tag{19}$$

where $K_1 \times K_2$ is the resolution of the constructed image. For each method, accuracy Acc refers to the average accuracy for the eight kinds of motor conditions and is defined as

$$\text{Acc} = \frac{\sum_{i=1}^{8} \text{Acc}_i}{8}, \tag{20}$$

where Acc_i is the validation accuracy of each fault type. This variable can be calculated as

$$\text{Acc}_i = \frac{N_S}{N_T} \times 100\%, \tag{21}$$

where N_S and $N_T = 100$ are the numbers of successful and the total tests, respectively. Here, TOP-1 accuracy is used to count the successful tests. That is, if the maximum probability of the predictive fault mode matches the actual fault mode, then the test will be considered successful.

The image resolution is selected from 7×7 pixels to 28×28 pixels, and the corresponding vibration signal length is selected from 98 sampling points to 1568 sampling points. The training data is obtained from the offline database and the validation data is acquired from the WSN in real time frame by frame. The data here and the data in figure 8(g) are in the same database. In figure 8(g), the signal length is 1452 sampling points, and the generated image is resized to 26×26 pixels for CNN training and validation. Besides the signal with a length of 1452 points, seven other kinds of signals with different lengths are tested to validate the overall performance of the proposed method. The validation accuracy of different methods under various resolution conditions is depicted in figure 16. Basically, the M1 curve is above the other curves in figure 16, which indicates that the proposed method achieves a better validation accuracy. For instance, the validation accuracy of the data with a 1452 signal length (corresponding to figure 8(g)) reaches 99.13%. This value is the highest out of all the methods with the same signal length, and hence demonstrates the superiority of the proposed method over other existing ones. From another aspect, the accuracy increases with the image resolution because a large image contains sufficient information relative to the motor condition. When the image resolution reaches 28×28 pixels, the accuracy of the M1, M2, M3 and M4 methods exceeds 98%, which is higher than that of M5. This result indicates that the image constructed through the TFA method contains more information than that constructed using the original time-domain signal.

When the image resolution or the signal length decreases, the accuracy of all the methods decreases accordingly. However, the accuracy remains higher in the proposed method M1 than in the other methods. In particular, the accuracy (without histogram equalization) is lower in M2 than in the proposed method with histogram equalization. This result explains that the histogram equalization can effectively improve the image contrast rate and further benefit feature extraction and fault type recognition. These experimental results demonstrate that the proposed method is effective and efficient for recognizing different motor fault types, especially when the vibration signal length from the WSN node is limited.

Table 5. Comparison of the transmission time, consumed energy, training and classification time for different image sizes and signal lengths.

Image resolution (pixels)	Signal length (samples)	Data transmission time (s)	Transmission consumed energy (J)	CNN training time (s)	CNN classification time (s)
7×7	98	0.057	0.020	2.33	0.081
10×10	200	0.115	0.039	2.67	0.108
12×12	288	0.165	0.057	3.33	0.115
14×14	392	0.225	0.077	4.33	0.133
18×18	648	0.371	0.127	6.00	0.143
22×22	968	0.554	0.190	7.67	0.173
26×26	1452	0.774	0.265	9.13	0.198
28×28	1568	0.898	0.308	11.67	0.211

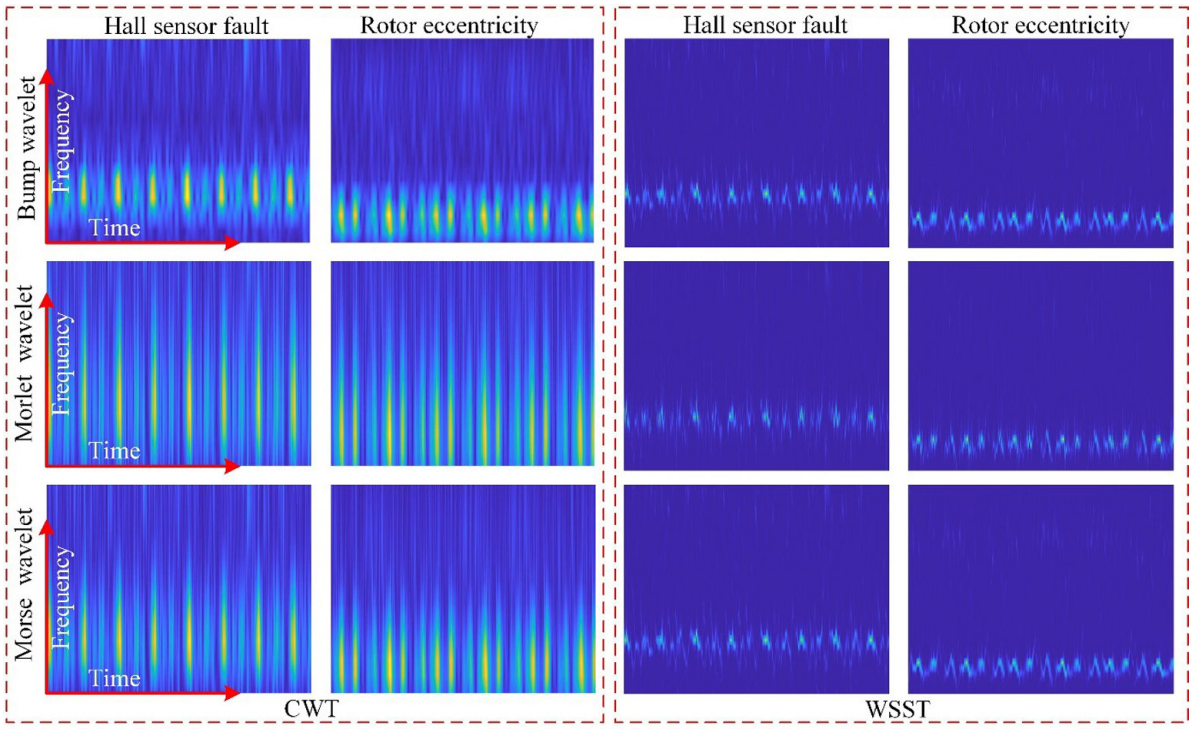

Figure 17. Comparison of different wavelets for the construction of time–frequency images.

6.2. WSN performance evaluation

The effectiveness and efficiency of the proposed method has been validated through the abovementioned experiments. Considering that the vibration signal is acquired and transmitted from the designed WSN node, the energy consumption and transmission time are evaluated to explain the use of the proposed method explicitly in practical applications. The statistical results are summarized in table 5. In the second column, data length represents the number of sampling points. Each sampling point occupies 2 bytes of storage space in accordance with the resolution of the ADC (16-bit). The third column measures the data transmission time from the transmitter and receiver of the WSN system. The baud rate of the transmitter/receiver is set to 9600 bit s^{-1}. The fourth column represents the total consumed energy of the transmitter and receiver calculated by multiplying the supply voltage and consumed current. The fifth column measures the CNN training time on the computer (configuration: Dual Core 2.30 GHz CPU, 8.00 GB RAM, 64-bit WIN10 Operation System, and MATLAB 2018b). The sixth column measures the execution time for each frame, including signal conversion, image enhancement and CNN classification.

In table 5, data transmission time and consumed energy increase nearly linearly with the image resolution and signal length because the transmitter/receiver operates in a stable mode. Because the size of the image data set is small (8000 samples) and the image resolution is low (maximal: 28×28 pixels), CNN training is fast on the computer. The classification time on the computer is small for all the cases, given sufficient computation resources required in executing a CNN algorithm. By comparing the results presented in figure 16 and table 5, a large image and a long signal length will increase the classification accuracy of the motor fault diagnosis and the consumed energy of the WSN. Thus, a trade-off between the accuracy and energy must be considered in motor fault diagnosis when the signal is acquired from a WSN with limited power supply.

Table 6. Comparison of the wavelets for CNN classification accuracy.

Bump + CWT	Morlet + CWT	Morse + CWT	Bump + WSST	Morlet + WSST	Morse + WSST
96.5%	94.75%	95.25%	98.25%	98.13%	98.25%

6.3. Discussions

In this study, the WSST constructs the images and then the CNN extracts the hierarchical features from the images. The wavelet function is a key factor that affects the TFA and image quality. In this subsection, the effects of the wavelet functions for image construction are investigated. Three wavelet functions including 'Bump', 'Morlet' and 'Morse' wavelets are used in both CWT and WSST methods for comparison, and the results are shown in figure 17. It can be found in the subfigures in the left panel (CWT method) that the 'Bump' wavelet has the best performance in characterizing the time–frequency features of the vibration signals. For instance, the periodic impulses in the vibration signals are highlighted, and the smearing phenomenon at frequency-axis in the 'Bump' subfigures is not that obvious compared with that in the 'Morlet' and 'Morse' subfigures. The results of the WSST method are shown in the subfigures in the right panel. It can be found that three different wavelet functions generate similar time–frequency images and these images have high definition in time–frequency planes. The synchrosqueezed process in the WSST re-distributes the energies at scales, and reduces the sensitivities of the time–frequency distribution coefficients, and finally improves the robustness and adaptivity of the wavelet transform.

In addition, the CNN classification accuracies based on the CWT and WSST in considering different wavelets are also calculated. The signal length and image resolution are configured as 968 points and 22×22 pixels, respectively. The results are shown in table 6. It can be seen in the first to third columns that the 'Bump' wavelet has the highest accuracy when the CWT is used to construct the images. This result is confirmed with the intuitional analysis in figure 17. For the results from the WSST method shown in the fourth to sixth columns, the 'Bump' and 'Morse' wavelets generate better results than the 'Morlet' wavelet. From another aspect, the accuracies from the WSST are all higher than those of the CWT, which confirms that a better image quality contributes better pattern recognition. The above results indicate that the proposed method including the WSST and histogram equalization steps are essential to obtain a high motor fault diagnosis accuracy, especially when the quality of the vibration signal is low due to the limitation of WSN.

7. Conclusion

This study proposes an enhanced feature extraction method to realize motor fault diagnosis using a vibration signal acquired from a WSN node. The proposed method contains four successive steps. (1) The vibration signal is acquired from an accelerometer installed in a motor and then transmitted to a computer through a WSN system. (2) A 1D vibration signal is converted to a 2D image through the WSST method. (3) The contrast rate of the constructed image is enhanced through histogram equalization. (4) A CNN model is designed and trained using the motor data set, and then the recognized motor fault is realized using the well-trained CNN model. The effectiveness of this method is verified on the BLDCM test rig with different types of motor faults. Moreover, the efficiency of the proposed method is validated by comparing it with other traditional methods. Considering that the data is acquired and transmitted from a WSN node, the relationship between the image resolution, data length, transmission time and consumed energy is investigated and discussed. The proposed method exhibits ensemble superiority to other methods when the vibration signal length is limited. Therefore, the proposed CNN method is suitable for remote motor fault diagnosis, especially when the motor signal is acquired and transmitted from a WSN with limited power supply.

Acknowledgments

This work was supported in part by the National Natural Science Foundation of China (Grant Nos. 51637001, 51605002 and 51675001), and in part by the Open Project Program of the Traction Power State Key Laboratory of the Southwest Jiaotong University (TPL1905), and in part by the Open Project Program of the State Key Laboratory of Mechanical Transmissions of the Chongqing University (SKLMT-KFKT-201812).

ORCID iDs

Siliang Lu https://orcid.org/0000-0002-7101-7948
Yongbin Liu https://orcid.org/0000-0002-3420-3784

References

[1] Nandi S, Toliyat H A and Li X D 2005 Condition monitoring and fault diagnosis of electrical motors—a review *IEEE Trans. Energy Convers.* **20** 719–29
[2] Guo J, Lu S, Zhai C and He Q 2018 Automatic bearing fault diagnosis of permanent magnet synchronous generator in wind turbine subjected to noise interference *Meas. Sci. Technol.* **29** 025002
[3] Wang X, Guo J, Lu S, Shen C and He Q 2017 A computer-vision-based rotating speed estimation method for motor bearing fault diagnosis *Meas. Sci. Technol.* **28** 065012
[4] Duran M J, Gonzalez-Prieto I, Rios-Garcia N and Barrero F 2018 A simple, fast, and robust open-phase fault detection technique for six-phase induction motor drives *IEEE Trans. Power Electr.* **33** 547–57
[5] He Q, Wu E and Pan Y 2018 Multi-scale stochastic resonance spectrogram for fault diagnosis of rolling element bearings *J. Sound Vib.* **420** 174–84
[6] Liu J and Shao Y M 2017 Dynamic modeling for rigid rotor bearing systems with a localized defect considering additional deformations at the sharp edges *J. Sound Vib.* **398** 84–102

[7] Wang D, Zhao X J, Kou L L, Qin Y, Zhao Y and Tsui K L 2019 A simple and fast guideline for generating enhanced/squared envelope spectra from spectral coherence for bearing fault diagnosis *Mech. Syst. Signal Process.* **122** 754–68
[8] Chen B J, He Z J, Chen X F, Cao H R, Cai G G and Zi Y Y 2011 A demodulating approach based on local mean decomposition and its applications in mechanical fault diagnosis *Meas. Sci. Technol.* **22** 115002
[9] Hu B B and Li B 2016 A new multiscale noise tuning stochastic resonance for enhanced fault diagnosis in wind turbine drivetrains *Meas. Sci. Technol.* **27** 025017
[10] Sun C, Ma M, Zhao Z B and Chen X F 2018 Sparse deep stacking network for fault diagnosis of motor *IEEE Trans Ind. Inform.* **14** 3261–70
[11] Shao H D, Jiang H K, Zhang H Z and Liang T C 2018 Electric locomotive bearing fault diagnosis using a novel convolutional deep belief network *IEEE Trans. Ind. Electron.* **65** 2727–36
[12] Sun W J, Zhao R, Yan R Q, Shao S Y and Chen X F 2017 Convolutional discriminative feature learning for induction motor fault diagnosis *IEEE Trans Ind. Inform.* **13** 1350–9
[13] Kang M, Kim J, Kim J M, Tan A C C, Kim E Y and Choi B K 2015 Reliable fault diagnosis for low-speed bearings using individually trained support vector machines with kernel discriminative feature analysis *IEEE Trans. Power Electr.* **30** 2786–97
[14] Qin Y, Wang X and Zou J Q 2019 The optimized deep belief networks with improved logistic sigmoid units and their application in fault diagnosis for planetary gearboxes of wind turbines *IEEE Trans. Ind. Electron.* **66** 3814–24
[15] Shao H D, Jiang H K, Zhang X and Niu M G 2015 Rolling bearing fault diagnosis using an optimization deep belief network *Meas. Sci. Technol.* **26** 115002
[16] Jia F, Lei Y G, Lin J, Zhou X and Lu N 2016 Deep neural networks: a promising tool for fault characteristic mining and intelligent diagnosis of rotating machinery with massive data *Mech. Syst. Signal Process.* **72–3** 303–15
[17] Han T, Liu C, Yang W and Jiang D 2019 Deep transfer network with joint distribution adaptation: a new intelligent fault diagnosis framework for industry application *ISA Trans.* accepted (https://doi.org/10.1016/j.isatra.2019.08.012)
[18] Jia F, Lei Y G, Lu N and Xing S B 2018 Deep normalized convolutional neural network for imbalanced fault classification of machinery and its understanding via visualization *Mech. Syst. Signal Process.* **110** 349–67
[19] Wang P, Ananya, Yan R Q and Gao R X 2017 Virtualization and deep recognition for system fault classification *J. Manuf. Syst.* **44** 310–6
[20] Wang H, Li S, Song L and Cui L 2019 A novel convolutional neural network based fault recognition method via image fusion of multi-vibration-signals *Comput. Ind.* **105** 182–90
[21] Huang R Y, Liao Y X, Zhang S H and Li W H 2019 Deep decoupling convolutional neural network for intelligent compound fault diagnosis *IEEE Access.* **7** 1848–58
[22] Shen C Q, Qi Y M, Wang J, Cai G G and Zhu Z K 2018 An automatic and robust features learning method for rotating machinery fault diagnosis based on contractive *Eng. Appl. Artif. Intell.* **76** 170–84
[23] Lei Y G, Jia F, Lin J, Xing S B and Ding S X 2016 An intelligent fault diagnosis method using unsupervised feature learning towards mechanical big data *IEEE Trans. Ind. Electron.* **63** 3137–47
[24] Zhao R, Yan R, Chen Z, Mao K, Wang P and Gao Robert X 2019 Deep learning and its applications to machine health monitoring *Mech. Syst. Signal Process.* **115** 213–37
[25] Lu S, Zhou P, Wang X, Liu Y, Liu F and Zhao J 2018 Condition monitoring and fault diagnosis of motor bearings using undersampled vibration signals from a wireless sensor network *J. Sound Vib.* **414** 81–96
[26] Niu J, Lu S, Liu Y, Zhao J and Wang Q 2019 Intelligent bearing fault diagnosis based on tacholess order tracking for a variable-speed AC electric machine *IEEE Sens. J.* **19** 1850–61
[27] Shi J J, Liang M, Necsulescu D S and Guan Y P 2016 Generalized stepwise demodulation transform and synchrosqueezing for time–frequency analysis and bearing fault diagnosis *J. Sound Vib.* **368** 202–22
[28] Thakur G, Brevdo E, Fuckar N S and Wu H T 2013 The Synchrosqueezing algorithm for time-varying spectral analysis: robustness properties and new paleoclimate applications *Signal Process.* **93** 1079–94
[29] Gonzalez R C 2008 *Digital Image Processing* 3rd edn (New Delhi: Prentice Hall India)
[30] Krizhevsky A, Sutskever I and Hinton G E 2012 Imagenet classification with deep convolutional neural networks *Neural Information Processing Systems (NIPS 2012, Lake Tahoe, NV)* pp 1097–105
[31] Abadi M *et al* 2016 TensorFlow: large-scale machine learning on heterogeneous distributed systems (arXiv:1603.04467)
[32] Xia M, Li T, Xu L, Liu L Z and de Silva C W 2018 Fault diagnosis for rotating machinery using multiple sensors and convolutional neural networks *IEEE/ASME Trans. Mech.* **23** 101–10
[33] Lu S and Wang X 2018 A new methodology to estimate the rotating phase of a BLDC motor with its application in variable-speed bearing fault diagnosis *IEEE Trans. Power Electr.* **33** 3399–410
[34] Wen L, Li X Y, Gao L and Zhang Y Y 2018 A new convolutional neural network-based data-driven fault diagnosis method *IEEE Trans. Ind. Electron.* **65** 5990–8